Biophysical Journal
Article

Biophysical Society

Lipid Order Degradation in Autoimmune Demyelination Probed by Polarized Coherent Raman Microscopy

Paulina Gasecka,[1] Alexandre Jaouen,[1] Fatma-Zohra Bioud,[1] Hilton B. de Aguiar,[1] Julien Duboisset,[1] Patrick Ferrand,[1] Herve Rigneault,[1] Naveen K. Balla,[1] Franck Debarbieux,[1] and Sophie Brasselet[1,*]
[1]Aix Marseille University, CNRS, Centrale Marseille, Institut Fresnel, Marseille, France

ABSTRACT Myelin around axons is currently widely studied by structural analyses and large-scale imaging techniques, with the goal to decipher its critical role in neuronal protection. Although there is strong evidence that in myelin, lipid composition, and lipid membrane morphology are affected during the progression of neurodegenerative diseases, there is no quantitative method yet to report its ultrastructure in tissues at both molecular and macroscopic levels, in conditions potentially compatible with in vivo observations. In this work, we study and quantify the molecular order of lipids in myelin at subdiffraction scales, using label-free polarization-resolved coherent anti-Stokes Raman, which exploits coherent anti-Stokes Raman sensitivity to coupling between light polarization and oriented molecular vibrational bonds. Importantly, the method does not use any a priori parameters in the sample such as lipid type, orientational organization, and composition. We show that lipid molecular order of myelin in the mouse spinal cord is significantly reduced throughout the progression of experimental autoimmune encephalomyelitis, a model for multiple sclerosis, even in myelin regions that appear morphologically unaffected. This technique permits us to unravel molecular-scale perturbations of lipid layers at an early stage of the demyelination progression, whereas the membrane architecture at the mesoscopic scale (here ~100 nm) seems much less affected. Such information cannot be brought by pure morphological observation and, to our knowledge, brings a new perspective to molecular-scale understanding of neurodegenerative diseases.

INTRODUCTION

The multilamellar myelin sheath wrapped around axons plays a crucial role for efficient transmission of nerve impulses, by acting as an electrical insulator (1). One of the most important features defining the functionality of myelin is the extraordinary ability of its components to self-assemble into a highly ordered and stable structure (2). This self-assembly is due to lipids (≈70% by dry weight) and proteins (≈30% by dry weight), which by interacting with each other form a tightly packed multilayered membrane with complex structure and lipid phases. In neurological disorders, this compact structure is highly perturbed (3,4), leading to dysfunctions of the central nervous system. Numerous studies of the sequence of the myelin sheath degradation process in the central nervous system have been reported (5,6), mostly concentrating on a murine model for multiple sclerosis, the experimental autoimmune encephalomyelitis (EAE). The reported general patterns are the enlargement of individual myelin sheaths, due to an interlamellar splitting and loss of bilayer adhesion, swelling, and finally the formation of vesiculated myelin debris (7,8).

Although the large malformations of the myelin ultrastructure in the advanced stages of demyelination have been reported, its finer structural variations at early stages remain poorly characterized, preventing a complete understanding of the molecular mechanism of myelin degradation in neurodegenerative diseases. So far, imaging techniques such as transmission electron microscopy (1) and small-angle x-ray diffraction (9,10) are used to access finer scales; however, they are highly invasive for the sample itself and lack of biochemical specificity is also an issue. In addition, there are growing indications that the morphological alterations occur in conjunction with molecular modifications, e.g., lipid composition (charged versus uncharged (11,12), saturated versus unsaturated (11,13)) or lipid phases (14–17) in the myelin sheath, which may contribute to the loss of lipid membrane interlayer adhesion, budding, and vesiculation (18).

Being able to image those fine structural or molecular alterations in the myelin sheath during degradation is thus

Submitted February 6, 2017, and accepted for publication July 26, 2017.
*Correspondence: sophie.brasselet@fresnel.fr
Editor: Arne Gericke.
http://dx.doi.org/10.1016/j.bpj.2017.07.033
© 2017 Biophysical Society.

CrossMark

of critical importance for a better understanding of the course of the demyelination progression. Among optical techniques that encompass optical coherent tomography (19), confocal reflectance (20), and nonlinear optics (21,22), coherent Anti-Stokes Raman scattering (CARS) microscopy is particularly interesting for its label-free nature, chemical specificity, and spatial resolution of a few 100 of nanometers. In CARS, a pump field (frequency ω_p) and a Stokes field (ω_s) interact with the sample to generate an anti-Stokes field at frequency $2\omega_p - \omega_s$, which is enhanced when $\omega_p - \omega_s$ is tuned to the resonant frequency of a Raman band (23–25). By addressing lipid molecules by their CH vibration bonds, which are highly abundant in the myelin sheath, CARS microscopy has been used to image myelin in the mouse brain (26,27), nerves of the peripheral nervous system (28,29), and spinal cord tissues (13,14,27,30–34) including during the progression of EAE (14,27,32). Using CARS images, the commonly used parameter in the assessment of the myelin health by its morphology is the g ratio, defined as the ratio between the inner and outer diameter of myelin fibers (14,28–30,33,35). This parameter, however, does not give any information on the possible molecular alterations. Furthermore, association of CARS with confocal Raman microspectroscopy has evidenced a higher degree of lipid unsaturation at sites of degraded pathological myelin, a feature that is associated with higher lipid-packing disorder (13). These findings suggest that lipid organization is affected in EAE tissues, even before any clear morphological sign of damage (13).

In this prospect, polarization-resolved CARS (PR-CARS) has been developed, which exploits the sensitivity of CARS to the coupling between incident excitation polarizations and the orientation of CH bond vibrations in lipids (36). In PR-CARS, the rotation of the incident pump and possibly Stokes linear polarizations generates a CARS signal modulation, which comes from the maximization of the CARS signal when the optical polarizations lie along the direction of the excited vibration modes (37). In lipid PR-CARS imaging in myelin, where CH_2 vibration modes are excited, this CARS modulation has been so far translated into a molecular order quantity supposing simple rigid lipid models (14,29,30,34,38). Although being simplified, this model allowed us to reveal changes of lipid organization due to demyelination in a murine model of Krabbe disease (38), or in developmental myelination in the zebrafish spinal cord (34). The rigid lipid model, however, does not reveal a quantitative and physical picture of the orientational behavior of lipids in complex environments such as myelin. First, it supposes a unique lipid symmetry, ignoring possible variations in lipid conformations and composition. Second, it limits the interpretation of angular order whereas another important piece of information lies in the phase of the CARS signal modulation, which represents the average direction of molecular bonds within the optical focus of excitation. This orientation information brings insights into possible local deformations of the membrane at mesoscopic scales (~100 nm below the diffraction limit size), where, for instance, membrane contour rupture or loss of lipid layer adhesion can occur. Such scales are particularly important in the context of demyelination processes where lipid membranes are packed into multilayer structures. In this work, we use a generic approach by analyzing the complete information accessible from PR-CARS experiments, revealing both lipid order microscopic and mesoscopic scale behaviors in demyelination processes occurring in neurodegeneration. For this, we use a more general symmetry decomposition supposing unknown orientational distribution of CH bonds (36,39,40). By using such an approach, we quantify the molecular order of CH bonds in myelin sheaths during active demyelination processes, as well as their averaged orientations, without any a priori knowledge on the lipid type, conformation, or membrane shape. We show that PR-CARS signal modulation can inform us not only on molecular scale disorder ultrastructure within the focal spot of optical resolution ~200 nm, but also at mesoscopic scales, which addresses modifications of molecular order over a distance of the image pixels size (typically ~100 nm). Performing PR-CARS analysis on spinal cord tissues taken from EAE mice at different stages of the disease, we show that early alterations of the myelin sheath occur at the molecular level, whereas the membrane architecture at the mesoscopic scale is seen to be particularly robust and mostly preserved until the formation of myelin debris. PR-CARS associated with such generic analysis is shown to be a potential tool for label-free early detection of demyelinating disease progression.

MATERIALS AND METHODS

EAE induction and sample preparation

All experimental procedures were performed in accordance with French legislation and in compliance with the European Community Council Directive of November 24, 1986 (86/609/EEC) for the care and use of laboratory animals. The research on animals was authorized by the Direction Départementale des Services Vétérinaires des Bouches-du-Rhône (license D-13-055-21) and approved by the National Committee for Ethics in Animal Experimentation (Section No. 14; project 87-04122012). C57Bl/6 mice were housed in cages with food and water ad libitum in a 12-h light/dark cycle at 22 ± 1°C.

EAE was induced in seventeen C57Bl/6 mice using MOG (35–55), a myelin oligodendrocyte peptide (75 μg in CFA, a complete Freund's adjuvant, containing 800 μg of killed *Mycobacterium tuberculosis*) by subcutaneous injection into three different locations (bilaterally over the femur, and at the base of the tail), and pertussis toxin (400 ng) by intraperitoneal injection on day 0 and 2. Additionally, a total of six control C57Bl/6 animals were used. Three of them received injections of an antigen-free emulsion (CFA containing 800 μg of killed *M. tuberculosis*), and pertussis toxin on day 0 and 2. First clinical signs typically arose 13–14 days postinduction and were translated into clinical scores as follows: 0, no detectable signs of EAE; 0.5, tail weakness; 1, complete tail paralysis; 2, partial hind limb paralysis; 2.5, unilateral complete hind limb paralysis; 3, complete bilateral hind limb paralysis; 3.5, complete hind limb paralysis and partial

forelimb paralysis; 4, total paralysis of forelimbs and hind limbs (mice with a score above 4.5 to be killed); and 5, death.

For the ex vivo sample preparation, groups of animals were sacrificed when reaching predetermined clinical scores for subsequent imaging of the myelin content in the dorsal spinal cord. Spinal cords were dissected, postfixed overnight at 4°C, and rinsed three times in phosphate-buffered saline before embedding in a 3% agarose matrix to ease handling and 3D positioning under the microscope. Care was taken to align the dorsal surface of the spinal cord with the upper surface of the agarose cube. Note that the fixation method did not affect the results presented in this work. A few measurements in fresh tissues were performed that revealed very similar data. The thickness of the whole spinal cord is 2 mm at the thoracic level; however, the depth penetration for CARS imaging is typically 40 μm in fixed and 80 μm in fresh samples, which is sufficient to study structures in the sensory tract parts of the neuronal network.

Multilamellar vesicles preparation

The multilamellar vesicles (MLVs) were prepared according to the Bangham (41) method. All phospholipids (1,2-dipalmitoyl phosphatidylcholine (DPPC), dioleoylphosphatidylcholine (DOPC), and cholesterol (Chol) were purchased from Avanti Polar Lipids (Alabaster, AL) and stored at −20°C. All lipids were dissolved in chloroform/methanol (9:1) to 10 mM concentration and mixed to prepare different lipid compositions: pure phospholipids, mixed with cholesterol solution at 5, 10, 20% (v/v), or used as ternary mixtures of ratios 1:1, 2:1, 2:1 DPPC/DOPC with 30% of cholesterol (v/v/v). First, 100 μL of these solutions were immediately evaporated under a nitrogen stream and then slowly dried in the nitrogen chamber for 1 h. The dried films were hydrated (1 h) above the main phase transition temperature, then gently shaken every 10 min. The hydration was performed in pure water (Milli-Q; Millipore, Billerica, MA) in the case of DPPC mixtures (T_m = 41.4°C), or in 1% agarose in pure water for DOPC (T_m = −17.3°C) and DPPC/DOPC/Chol mixtures (T miscibility ∼30°C (42)) to prevent MLVs motion. A small amount of the obtained suspension was placed between two coverslips separated by 100-μm spacers. In the case of DOPC/Chol and DPPC/DOPC/Chol mixtures this suspension was gently heated above the gelling temperature of agarose (∼25°C) before use. PR-CARS data were recorded at room temperature (21°C), in the spectral region predominantly dominated by CH_2 and CH_3 stretching vibrations, using the same conditions as for myelin samples. We considered MLVs having comparable intensity and size in the range from 5 to 30 μm, concentrating on pixels at the periphery of the MLVs. Note that various MLV morphologies could be observed due to the intrinsic heterogeneity of the preparation method. We discriminate in particular filled MLVs that contain visible lipid signal in their center, and nonfilled MLVs that might be deprived of lipids at their center and thus support higher membrane tension.

PR-CARS imaging

PR-CARS imaging (represented in Fig. 1 *A*) was done using an OPO femtosecond laser source (80 MHz 150 fs; Coherent, Santa Clara, CA) with excitation wavelengths λ_p = 830 and λ_s = 1087 nm, temporally synchronized and spatially overlapped on the sample plane. The corresponding excited resonances correspond to lipid vibrations around 2850 cm^{-1} with a bandwidth 150 cm^{-1}, dominated by the CH_2 and CH_3 stretching modes. The total power delivered to the sample is in the range of 10 mW, focused by a water immersion objective (40×/1.15W; Nikon, Tokyo, Japan), which provides an optical resolution of ∼250 nm. Imaging is performed in the epi-inverted microscope geometry, using the dichroic mirror T770SPXR (Chroma Technology, Bellows Falls, VT). The scanning mirror rate is 20 μs per pixel, over 30-μm size images (200 × 200 pixels). The nonlinear signal collected by the objective is filtered using a short-pass filter (ET750sp-2p8; Chroma Technology) before being detected by a PMT (R9110; Hamamatsu, Shizuoka, Japan) in the spectral range of 650 nm using a bandpass filter

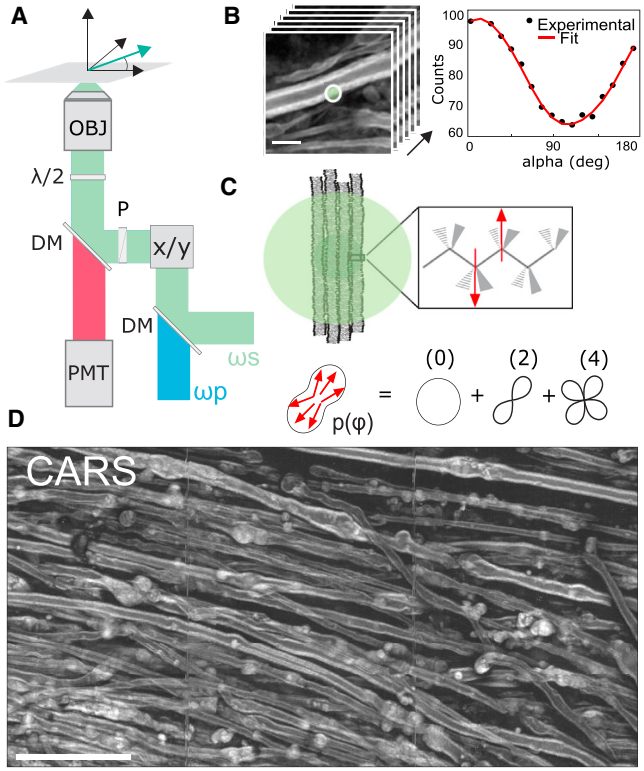

FIGURE 1 (*A*) Schematic view of the PR-CARS microscope. The vector ***E*** represents the direction of linear polarization of ω_s and ω_p (α-angle), rotated by a half-wave plate (λ/2). DM, dichroic mirror; *x*/*y*, galvanometric mirrors; P, polarizer; PMT, photomultiplier tube; OBJ: objective. (*B*) Given here is an example of PR-CARS data (*left panel*) recorded in one pixel (*right panel*) of the myelin sheath region (control sample), averaged over the diffraction limit size (schematically represented by a *circle*). Scale bars represent 5 μm. (*C*) (*Top*) Given here is a schematic of the multilamellar lipid membrane in the focal spot (represented as a *circle*) and zoom on a lipid showing the dominant nonlinear bond dipoles (*arrows*) probed by PR-CARS. (*Bottom*) Distribution function $p(\varphi)$ is read-out from PR-CARS (see text), as a sum of orders of symmetry. (*D*) Given here is a large-scale CARS image (total intensity summed over 18 input polarization angles) of a spinal cord tissue (score 1.5). Scale bars represent 50 μm. To see this figure in color, go online.

655AF50 (Omega Optical, Brattleboro, VT). Polarization imaging is done by rotating the linear polarization angle of the incoming beam in 10° steps over the range 0°–170° (Fig. 1 *B*), using an NIR achromatic half-wave plate (AHWP05M-980; Thorlabs, Newton, NJ) mounted in a motorized rotation mount (PR50CC; Newport, Irvine, CA). An image is recorded at each polarization step as explained in (43). This results in a polarimetric image stack (Fig. 1 *B*) where each pixel contains a PR-CARS modulated response.

Data processing and analysis

The quantification of molecular order from PR-CARS measurements was previously described in (39,40). Briefly, both linearly polarized incident pump (E_p) and Stokes fields (E_s) are rotated with a variable angle α relative to the sample plane horizontal axis *X* (Fig. 1, *A* and *B*). The PR-CARS response is then analyzed to retrieve orientational parameters from the lipid assembly present in the focal volume of the objective. The PR-CARS signal is derived from a bond additive model where individual CH molecular

bonds (represented as *arrows* in Fig. 1 *C*) form the excited vibrational modes. These molecular bonds are organized into a 2D effective distribution function $p(\varphi)$, which can be decomposed over its symmetry orders (Fig. 1 *C*):

$$p(\varphi) = p_0 + p_2\cos(2\varphi) + q_2\sin(2\varphi) + p_4\cos(4\varphi) + q_4\sin(4\varphi), \quad (1)$$

where p_0 is the isotropic contribution to the angular distribution, (p_2, q_2) are its second-order symmetry components, and (p_4, q_4) are its fourth-order symmetry components. This decomposition allows us to avoid any hypothesis on the measured vibrational modes population, which could come from different types of lipids and different lipid conformations.

The molecular bonds add up coherently to form the CARS nonlinear coherent radiation, which intensity is decomposed on a circular basis (see Supporting Material):

$$I^{\mathrm{CARS}}(\alpha) \propto a_0 + a_2\cos(2\alpha) + b_2\sin(2\alpha) + a_4\cos(4\alpha) + b_4\sin(4\alpha) + a_6\cos(6\alpha) + b_6\sin(6\alpha). \quad (2)$$

The (a_n, b_n) coefficients are directly calculated from the recorded polarization-dependent image stack, by projection on circular basis functions.

In the PR-CARS data analysis, the (p_n, p_n) parameters are then deduced from the (a_n, b_n) coefficients following the relations derived in (39,40) (see Supporting Material). To define the properties of the distribution function parameters measured for each pixel of the PR-CARS image, we introduce the magnitudes (S_2, S_4) and orientations (φ_4, φ_4) of the second and fourth symmetry order contributions, respectively:

$$S_2 = \frac{1}{p_0}\sqrt{p_2^2+q_2^2};\ S_4 = \frac{1}{p_0}\sqrt{p_4^2+q_4^2}, \quad (3)$$

$$\varphi_2 = \begin{cases} \frac{1}{2}\arctan(q_2/p_2), & \text{if } p_2 > 0 \\ \frac{1}{2}\arctan(q_2/p_2) + \frac{\pi}{2}, & \text{else} \end{cases}, \quad (4)$$

$$\varphi_4 = \begin{cases} \frac{1}{4}\arctan(q_4/p_4), & \text{if } p_4 > 0 \\ \frac{1}{4}\arctan(q_4/p_4) + \frac{\pi}{4}, & \text{else} \end{cases}. \quad (5)$$

The anisotropic nature of an angular distribution function is mainly quantified by its contribution S_2 and main orientation φ_2, whereas S_4 and φ_4 quantify the shape (smooth versus sharp) of this distribution. It is convenient to rewrite S_4 as a symmetric component that is of cylindrical symmetry along φ_2 (denoted $S_4^{(s)}$) and an asymmetric contribution (denoted $S_4^{(s)}$) (44):

$$S_4^{(s)} = S_4\cos[4(\varphi_4-\varphi_2)];\ S_4^{(a)} = S_4\sin[4(\varphi_4-\varphi_2)]. \quad (6)$$

In particular, if the distribution is of cylindrical symmetry, then $\varphi_2 = \varphi_4$ or $\varphi_2 = \varphi_4 \pm 45°$, and $S_4^{(s)} = 0$. Theoretical analyses on modeled angular distribution functions show that the parameters (S_2, $S_4^{(s)}$, $S_4^{(a)}$) permit us to discriminate between different shapes of molecular angular distributions (39,44).

In practice, the selection of the relevant pixels to be analyzed is performed on the basis of the total CARS intensity image obtained by summing for each pixel the signal obtained for all angles α. To perform intensity thresholding based on criteria discussed below, the PR-CARS intensity is averaged over 3×3 pixels, and only pixels where total intensity is above 75% of the threshold are considered. Pixels corresponding to the signal from the myelin sheath and its different morphological variations are manually selected using a polygon selection tool of MATLAB (The MathWorks, Natick, MA). For the estimation of the *g*-ratio parameter in straight myelin sheaths, the *g*-input function of MATLAB is used. We made sure that the myelin sheath regions selected to calculate the molecular order parameters correspond to *g*-ratio values within a range of 0.05 relative to the mean *g*-ratio of the given population. The retrieved molecular order parameters (S_2, $S_4^{(s)}$, $S_4^{(a)}$) are indicated with their mean and SD values, measured over a large collection of myelin sheath regions for each given population. Statistical significance was determined using ANOVA tests performed over those populations with *, $p \leq 0.05$ considered as statistically significant; **, $p \leq 0.01$ as highly statistically significant; and ***, $p \leq 0.001$ as extremely statistically significant.

RESULTS

Fig. 1 *D* shows a typical CARS image of myelin sheaths in a mouse spinal cord, imaged at ~20–30 μm below the spinal cord surface with linear polarization excitation along the spinal cord axis. The CARS signal is dominated by symmetric and antisymmetric CH_2 stretching vibrations of hydrocarbon chains from lipids (2845 and 2885 cm^{-1}, respectively), which are the major components of myelin. CH_3 stretching vibration of proteins (2930 cm^{-1}) also contribute to a lesser extent, because they constitute 15–30% of the weight of the myelin sheath (13,14). Fig. 1 *D* and the zoomed view of Fig. 1 *B* show longitudinal sections of lipid multilayers of ~3–5 μm in total diameter, wrapped around axons. The myelin morphology is seen to be strongly affected when the EAE score disease increases, from straight myelin tubular structures to swelled features (appearing at score 1) coming from vesiculated myelin, and finally to the formation of debris with spherical shapes of various sizes, coming from disrupted myelin detached from the axon (with a major proportion at scores 2.5 and 4).

Molecular order of lipids in the myelin sheath

A PR-CARS polarization analysis has been performed on zoomed-in regions of the myelin sheath structure, using a high sampling pixel size of 100 nm. Fig. 2 shows typical PR-CARS results in a spinal cord of a control tissue.

The interpretation of the measured (S_2, $S_4^{(s)}$, $S_4^{(a)}$) values depicted in Fig. 2, *B–D*, requires a rigorous control of measurement conditions to avoid bias and error sources (see Supporting Material). Briefly, the intensity level is set above a threshold that guarantees SD of S_2 <0.02, and of ($S_4^{(s)}$, $S_4^{(a)}$) <0.08 (see Fig. S1). A residual but not significant intensity-dependent bias is also systematically removed (see Fig. S1). The S_2 values additionally suffer from a bias due to the presence of nonresonant background (40), which can be tolerated in relative comparison studies and therefore

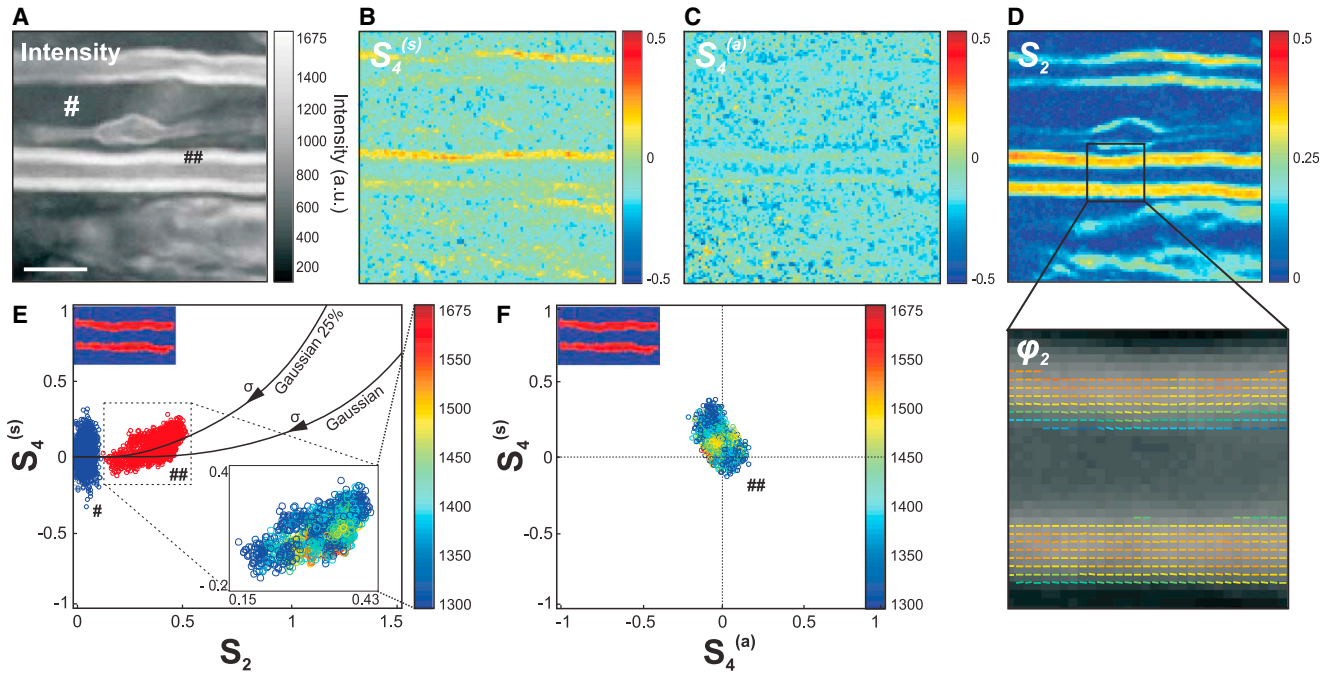

FIGURE 2 (*A*) Given here is a PR-CARS (centered at 2845 cm^{-1}) total intensity image (sum over 18 input polarization angles) of the myelin sheath from a spinal tissue (control sample). Scale bars represent 5 μm. (*B*) Given here is a corresponding $S_4^{(s)}$ map. (*C*) Given here is a $S_4^{(a)}$ map. (*D*) Given here is a S_2 map. For those maps (not for data analysis), the PR-CARS intensity is averaged over 3×3 pixels. A region of the S_2 map is zoomed-in to make more visible the complete orientational information, represented by a stick oriented with the φ_2 angle with respect to the horizontal axis, and which color is S_2. (*E*) Given here are experimental values of S_2, $S_4^{(s)}$ taken at intensities above the threshold 1300 analog signal value in the myelin sheath (## in the intensity image (*A*)) and at lower intensity signals from a surrounding background (# in the intensity image (*A*)). For the myelin sheath region, the inset image is color-coded in intensity. (*Solid lines*) Given here are theoretical (S_2, $S_4^{(s)}$) values for a Gaussian distribution of increasing width σ, and Gaussian superimposed with an isotropic distribution of proportions 25%. (*F*) Given here is a $S_4^{(a)}$,$S_4^{(s)}$ scatter plot following a similar color-coded intensity scale to that in (*E*). To see this figure in color, go online.

not removed. Another source of bias can also occur due to the out-of-plane orientation of the measured distributions, S_2 values being at their maximum when the distribution lies in the sample plane. This effect is excluded by a control of the plane of focus at the equatorial plane of the myelin sheath (see Fig. S2). At last, birefringence is seen to lead to negligible bias of the deduced values at the depths of measurement used in this analysis (see Fig. S3). Note that scattering from the spinal cord tissue can also be neglected; previous studies have indeed shown that effects due to the detected multipally scattered light in epi-geometry do not affect the polarization CARS signals as long as the total intensity (nonanalyzed detection) is recorded (45).

The S_2 image is strongly contrasted (Fig. 2 *D*), which is consistent with the tight packing of lipids in the multilamellar structure of myelin, whereas the background is isotropic ($S_2 = 0$). The φ_2 image (Fig. 2 *D*) shows additionally that the general orientation of CH bond dipoles in the equatorial plane is along the myelin tubular axis, as expected from lipid chains oriented radially in a concentric axonal structure. The fourth-order symmetry of the CH bonds distribution provides additional information, because $S_4^{(s)}$ is clearly above the surrounding background (Fig. 2, *B* and *E*). The (S_2, $S_4^{(s)}$) experimental values are plotted together as a scatter graph in Fig. 2 *E* to provide a finer interpretation of the CH bonds' orientational distribution in the lipid multilamellar structure. Importantly, the measured order parameters are seen to not depend on the intensity (Fig. 2 *E*), which excludes experimental artifacts related to noise level. Continuous lines on this graph represent theoretical dependencies expected from different orientational distributions of CH bonds that span similar regions as experimental values. For a Gaussian distribution of width σ, S_2 is expected to grow with decreasing σ, without considerable increase of $S_4^{(s)}$ except at low widths ($\sigma < 80°$). The measured $S_4^{(s)}$ values are, however, higher than expected from a Gaussian distribution. This can be explained by the presence of an isotropic angular population superimposed to a Gaussian function (44), which could occur from small disordered regions in the focal volume, such as subdiffraction size vesicles. Fig. 2 *E* depicts different cases of distributions composed of η% of an isotropic population superimposed with $(100 - \eta)$% of a Gaussian population, showing that the measured values correspond to $\eta \approx 25\%$ (accounting for the fact that S_2 is probably slightly underestimated due to the presence of nonresonant background). At last, $S_4^{(a)} \approx 0$ (Fig. 2, *C* and *F*), confirming the cylindrical symmetry of the orientational distribution of bonds in the

lipid organization. In what follows, S_4 will often be used as a shortened notation for $S_4^{(s)}$, and $S_4^{(a)}$ will be discarded.

Overall, the average values $\langle S_2 \rangle = 0.33 \pm 0.05$ and $\langle S_4 \rangle = 0.10 \pm 0.07$ obtained in the myelin sheath depict a molecular order contained in an angular width of $\sim\sigma \approx 80^\circ$. Interestingly, this order is not far from that observed in model membranes; PR-CARS performed in MLVs made of pure lipids indeed show that $\langle S_2 \rangle \approx 0.22$ in DOPC MLVs and $\langle S_2 \rangle \approx 0.40$ in DPPC MLVs (see Fig. S4), the latter exhibiting a higher liquid-order phase transition temperature. The presence of several lipid types and proteins in the myelin sheath visibly does not enlarge considerably the CH bonds angular distributions as compared to MLVs, confirming the tight organization of lipids along the axons. Looking closer at SD, however, the orientational behavior of CH bonds exhibits a higher level of heterogeneity per sample than in MLVs (see Fig. S4), which is coherent with their diversity and the complexity of the interlamellar interactions in myelin.

Relation between lipid packing orientational order and myelin morphology

During demyelination, the compact multilamellar structure of myelin undergoes swelling and degradation, until the formation of detached debris. In this section, we investigate if there is a correlation between the morphology of the myelin sheath and lipid order measured by PR-CARS, regardless of the score of the EAE disease progression. A more quantitative comparison between scores will be given in the next section.

PR-CARS measurements were performed at different stages of the EAE disease progression in mice, from control to score 4. CARS imaging was first performed to localize areas on fixed spinal tissues, chosen randomly over several millimeter distances. Second, PR-CARS was performed in several small regions of interest (ROIs) (typically 20 μm $\times$ 20 μm size) at various places. CARS images permitted us to determine five categories that are considered as representative of the different characteristic morphological features observed during the demyelination process, depicted in Fig. 3 *A*: normal myelin has a compact structure, with visible straight borders forming a tubular structure around the axon; swollen myelin defines more loose membrane formations. The term "blebbed" denotes a later stage of swelling, which forms a more pronounced protrusion outside of the straight myelin sheath structure; the term "debris" denotes a lipid multilamellar spherical structure from vesiculated myelin, which has detached from the myelin sheath. Such debris, reported in the literature (7,8), are found in two categories: "nonfilled debris", which show no lipid signal at their center, and "filled debris", which are pure lipid volumetric structures. We observed an increased amount of damaged or vesiculated myelin with the progression of the disease as previously reported (13,32).

For each category, we measured molecular order of CH bonds, deducing (S_2, S_4) from PR-CARS data. We did not observe significant changes of S_4 in this study, therefore this parameter is omitted in what follows. Fig. 3 *B* (*left*) depicts zoomed-in images of the S_2 parameter measured on each type of category. The S_2 histograms (Fig. 3 *B*, *middle*) collected for each of those characteristic regions illustrate the heterogeneity of molecular order in degraded myelin. The mean orientation (φ_2) as represented in these regions (Fig. 3 *B*, *right*) depicts the spatial properties of such molecular order in both healthy and damaged regions.

A few key observations can be made. 1) The average S_2 values decrease from normal ($S_2 \approx 0.30$) to swollen ($S_2 \approx 0.25$) and blebbed ($S_2 \approx 0.17$) myelin, indicating loss of molecular scale order. Fig. 3 *C* depicts such situations schematically, supposing that this disorder originates purely from morphological nanometric scale perturbations. 2) In blebbed and debris structures, S_2 is more heterogeneous than in normal structures, with lower molecular order at the inner edge of the membrane. 3) Molecular order in debris is preserved at their edge, with only inner membranes perturbed with high disorder (lipid order in the periphery of not-filled debris is rather high as compared to filled debris, similarly to what has been observed in DPPC MLVs in which the filled structures exhibit a lower molecular order; see Fig. S4). In not-filled debris, CH molecular order can even reach values measured in normal myelin sheaths. 4) The overall orientation of CH bonds, illustrated by (S_2, φ_2) images, seems to follow the membrane macroscopic direction whatever the disorder, even for low S_2 regions where the molecular scale disorder is high. This indicates that at the mesoscopic scale represented by the pixel size (here 100 nm), no strong modification of the membrane structure is found, whereas disorder is still rather occurring at a molecular/nanometric scale, averaged within the focal sport size. Overall, these observations show that the transformation of normal, compact myelin structure into the final debris results in important local nanometric rearrangements of the multilamellar membrane structure, which seem to be able to persist over mesoscopic scale distances.

The values of molecular order measured here for a given region, stay valid over a large population of regions. Measurements performed on 359 regions (on average, 70 regions per category) are summarized in global histograms in Fig. 4 *A*. Independent of the stage of the EAE disease, normal myelin exhibits the highest degree of lipid packing ($\langle S_2 \rangle = 0.32$), which corresponds to the smallest aperture σ of the effective distribution function $\approx 80^\circ$. The degradation of lipid packing in the myelin lamellar structure of swollen regions is manifested by a decrease down to $\langle S_2 \rangle = 0.23$, which correspond to an aperture σ of $\approx 100^\circ$. In blebbed myelin, the averaged global order goes down to $\langle S_2 \rangle = 0.14$ ($\sigma \approx 120^\circ$), mainly due to the strong disorder observed inside their structure. Concerning myelin degeneration products, the outer membrane of not-filled debris

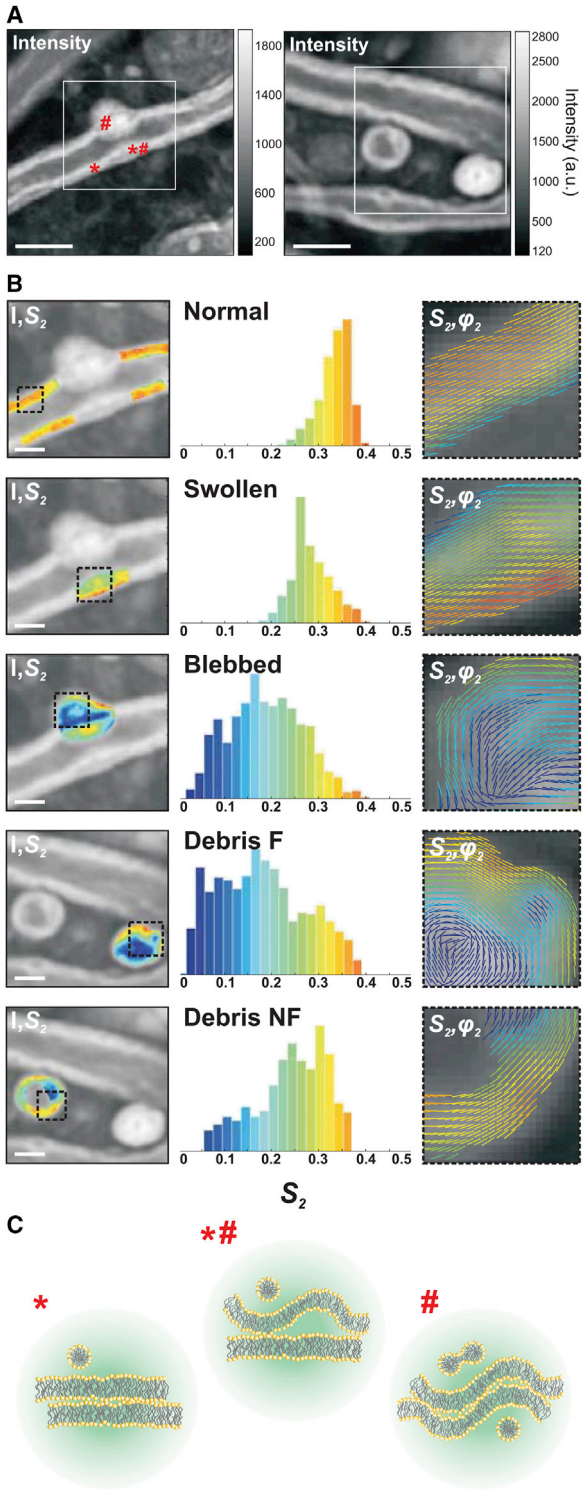

FIGURE 3 PR-CARS analysis of the different characteristic morphological features visible in the demyelination process. (*A*) Total intensity images were taken from clinical score 1 (*left*) and 2 (*right*). Symbols (*, #, *#) refer to different membrane locations. White square ROIs are used for statistical analysis in (*B*). Scale bars represent 5 μm. (*B*) (*Left*) Given here are S_2 maps (superimposed on the intensity image) of characteristic features of myelin degradation in white ROIs of (*A*): "healthy" myelin, "swollen", and "blebbed"; and products of degradation: "debris not filled (*NF*)" and "debris filled (*F*)". (*Middle*) Given here are corresponding histograms of S_2 values, taken within the dashed square ROIs in (*B*). (*Right*) Given here are combined images of S_2 and φ_2, showing S_2 as a color scale and φ_2 as the orientation of sticks for each measured pixel. (*C*) Given here is a schematic morphological interpretation of the myelin multilayer (enlarged) in positions in (*A*) corresponding to (*) "healthy", (*#) "swollen", and (#) "blebbed" myelin. The circular region represents the focal spot (not to scale). To see this figure in color, go online.

exhibits an averaged order of $\langle S_2 \rangle = 0.25$, which is higher than for filled ones $\langle S_2 \rangle = 0.17$. All cases show significant differences between each other, except for not-filled debris, which resemble swollen myelin.

The heterogeneity of molecular order within these regions is seen to increase for degraded myelin, as compared to normal myelin (Fig. 4 *B*). The SD of S_2 (σ_{S_2}) shows that in normal myelin, a low SD is measured ($\sigma_{S_2} = 0.06$). This value is not noise-limited (as visible in the low background value where $\sigma_{S_2} = 0.03$), but still characteristic of very homogeneous lipid packing. From normal to debris, this SD increases with $\sigma_{S_2} = 0.08$ in swollen, blebbed myelin and not-filled debris, and $\sigma_{S_2} = 0.09$ in filled debris. The filled debris regions indeed exhibit a very wide histogram, mostly due to the fact that, in these structures, the inner membrane shows very disordered characteristics.

Evolution of lipid organization in the myelin sheath with the progression of EAE

The different myelin morphological features described above, which characterize demyelination, were visible in all samples independently of the EAE clinical score, even though their occurrences varied from score to score. In this section, we evaluate how S_2 values in these different regions depend on the clinical scores of EAE. This should allow an assessment of the finer evolution of myelin microscopic-scale properties during neurodegeneration. For each measured score, two spinal cords have been imaged with an equal number of regions per spinal cord, except for score 4, where only one spinal cord was measured. Additionally, injection of complete Freund's adjuvant (CFA sample) was produced to evaluate the consequence of the induction of an inflammation that is not specific to EAE.

First, normal myelin can be classified depending on the thickness of its sheath. For this, we quantified the *g* ratio of all measured normal-looking myelin sheaths, defined by the ratio between the inner to the outer diameter of the myelin membrane (see Fig. S5). Fig. 5 *A* shows that *g*-ratio values are found to be in the range 0.3–0.65, which is consistent with what has been reported in the literature (14,30,33). Only a slight correlation between the *g* ratio and $\langle S_2 \rangle$ values was visible over all measured samples (see Fig. S5). The variation of *g*-ratio values for the different clinical scores of EAE was seen to be very large even inside a given score population (Fig. 5 *A*). Note that the high value measured for CFA samples might be due to myelin swelling

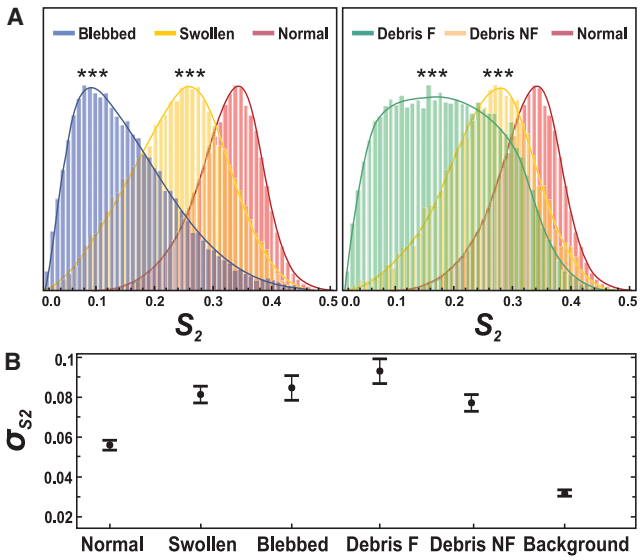

FIGURE 4 (*A*) Given here are general normalized histograms (over all measured pixels) of characteristic features of myelin degradation plotted for all measurements, regardless of the clinical score of the EAE disease (~1000 pixels per regions). Number of regions measured: normal myelin ($N = 136$), swollen ($N = 91$), blebbed ($N = 82$), debris filled (F) ($N = 30$), debris not-filled (NF) ($N = 20$). ***, $p \leq 0.001$. (*B*) Given here are corresponding SD σ_{S_2} values within each region, taken per category. Error bars are SD values over all regions measured. To see this figure in color, go online.

as a result of the immune response to the injection. Contrary to previous works (28,46) that observed the thinning of myelin sheath (decrease of the g ratio), we do not observe a drastic trend of dependence between g ratio and a normal-appearing myelin condition during the progression of EAE.

In contrast, more pronounced variations were observed in S_2 values measured in myelin sheaths of normal morphology for different EAE clinical scores (Fig. 5 *A*). S_2 values in normal myelin morphologies decrease progressively from 0.31 ± 0.03 (control sample) down to 0.26 ± 0.04 (score 2.5). All values show statistically significant changes as compared to the control sample, except scores 1.5 and 4, which are poorer in statistics. Note that score 4 contains a very low number of healthy-looking myelin sheaths, therefore the high S_2 values measured are probably originating from the few robust myelin sheaths that survived the progression of the disease. The CFA sample exhibits a difference with the control sample and similarly with score 1, which increases when comparing CFA with score 2. This suggests that pure immune reaction due to the injection provokes slight modifications of lipid order in myelin, but the loss of molecular order due to EAE remains significant. Moreover, no significant difference is observed in-between scores except between scores 0 and 2. These data show overall that molecular order in the myelin sheath of normal morphology decreases at the early stage of the clinical signs of the EAE disease. Note that this trend is also visible when taking all myelin morphology types together, although in this case the S_2 population might contain regions dominated by isotropic disorder present in myelin blebs and debris, making the error margins larger.

At last, PR-CARS measurements of normal myelin at different EAE scores were compared with artificial multilamellar lipid membranes of different compositions, to evaluate lipid order behaviors in myelin with respect to known systems. Fig. 5 *B* shows that on average, normal myelin sheaths visible in the different observed EAE scores exhibit (S_2, $S_4^{(s)}$) values close to DOPC/Chol MLVs mixtures with a high content of cholesterol (20%). The loss of lipid order between the control sample and score 2 is similar in magnitude to that induced in DOPC between high cholesterol content and no cholesterol. Interestingly, much higher shifts of S_2 values were visible when varying cholesterol content above 5% in DPPC MLVs, or when varying the DPPC/DOPC ratio in lipid mixtures, demonstrating the high sensitivity of saturated lipid order to their local environment. These results

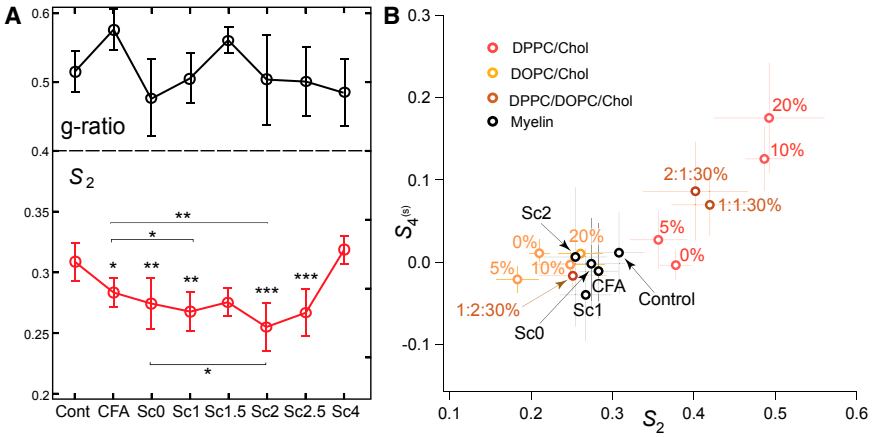

FIGURE 5 (*A*) (*Top*) Given here are mean g-ratio values versus the EAE score (see Fig. S5). (*Bottom*) Given here are S_2 values versus different scores of EAE, for the myelin regions of normal morphology (see text). Statistical analysis is shown relative to the control sample except when notified with a bar (*, $p \leq 0.05$, **, $p \leq 0.01$, ***, $p \leq 0.001$). Given is the number of regions considered in the analysis: control ($N = 26$), CFA ($N = 30$), score 0 ($N = 28$), score 1 ($N = 17$), score 1.5 ($N = 9$), score 2 ($N = 22$), score 2.5 ($N = 19$), score 4 ($N = 11$). Error bars are SD values. (*B*) Shown here are (S_2, $S_4^{(s)}$) values for myelin at different EAE scores (straight myelin sheaths are considered, and only the most statistically relevant scores are depicted for clarity) and MLVs from different lipid/cholesterol compositions: pure DPPC/Chol or DOPC/Chol at 0, 5, 10, 20% (v/v), or DPPC/DOPC/Chol 30% (v/v/v) ternary mixtures with DPPC/DOPC ratios 1:1; 1:2; 2:1. Error bars are SD values (for MLV samples $N = 4$). To see this figure in color, go online.

overall show that the magnitude of lipid order loss produced in EAE samples does not reach the level of loss induced by modifications of saturated lipid systems. At last, comparison with mixtures of DPPC/DOPC/Chol (30%) samples show that the closest system to which EAE has high-scores of myelin would be 1:2:Chol (30%), here again favoring a similarity with preferentially unsaturated lipids systems. The control sample, on the other hand, is approaching a mixture containing a higher portion of saturated lipids.

DISCUSSION

Measuring molecular order in the myelin sheath by PR-CARS clearly permits us to assess features in tissues that are not visible by pure (non-PR) CARS imaging. The measurements performed highlight in particular that in the EAE demyelination process, the lipid multilayers organization of the myelin sheath is perturbed at a molecular/nanometric scale (as seen on S_2 images), especially in the inner membrane region of the myelin sheath and from normal to swelled/blebbed myelin. This brings, to our knowledge, new elements of information to the understanding of lipid membrane behaviors in neurodegenerative diseases, which has been a topic of strong interest for decades. It has been reported that in the EAE pathology, different factors can contribute to the demyelination process, which cover molecular composition modifications and nanometric-scale morphological changes. Even though PR-CARS microscopy cannot distinguish between those two factors, quantitative elements can be gained from the measured modifications of lipid molecular order.

First, existing observations in EAE samples have shown that lipid integrity (charge, degree of saturation, cholesterol content) is altered, which leads to an increase in membrane fluidity and to a decrease of myelin adhesion that provokes vesiculation (11,13). Our PR-CARS analyses show a loss of lipid order induced by EAE that is similar in magnitude to a high loss of cholesterol content (20–0%) in unsaturated lipid vesicles. This is consistent with the unsaturated nature of lipids in myelin but not with the increase in cholesterol content previously reported (11,47). Note that this comparison is only partial because proteins, in particular myelin basic protein that participates in lipid layers adhesion, are absent in model lipid membranes. Nevertheless, the PR-CARS results show that despite its higher complexity, myelin lipid order is still close to that found in model unsaturated lipid systems and that lipid composition modifications seen in the EAE progression are likely to not be a major source of lipid order change in myelin. The origin of the observed loss of order could be rather dominated by local morphological effects as discussed below, which are a direct consequence of lipid composition changes.

Second, the membrane morphology of myelin is likely to be affected at the nanometric scale, as known from x-ray diffraction (47) and electron microscopy studies (1). Numerical models in PR optical microscopy have shown that increasing a single lipid membrane curvature can lead to significant changes in the read-out of the S_2 parameter. Typically, a 10-nm height change within the diffraction-limited spot of 200 nm leads to an increase of S_2 of 0.1 (48). Reported local folding in demyelination processes, using x-ray diffraction, have shown an increase of spacing between bilayers ($\approx$6–7 nm as compared to $\approx$3–4 nm in healthy myelin) during the swelling process (47). Our data suggest a decrease of S_2 from normal to swollen of $\sim$0.1 that could be consistent with such a small morphological modification. It is in particularly likely that the PR-CARS measurements probe perturbations from well-stacked parallel layers in normal myelin (* in Fig. 3 *A*) to partly folded interlayer membrane regions in swollen myelin (*# in Fig. 3 *A*), and finally to completely folded multilayer membrane regions in the interior of blebbed myelin (# in Fig. 3 *A*).

More information can be gained from the averaged orientation of the CH bond organization (φ_2 images). Interestingly, even though molecular order can be strongly affected locally, the averaged orientation of molecular bonds still follows the macroscopic membrane direction. This means that even though the perturbation occurs at the molecular scale (lipid composition and interaction changes) or at the nanometric scale (subdiffraction membrane folds), the membrane cohesion is preserved at the mesoscopic scale ($\sim$100 nm pixel size) (Fig. 3 *B*). Long persistence lengths of φ_2 values are clearly visible whatever the degree of nanometric scale disorder in the local membrane, which could also explain the capacity of such local disruptions to create longer scale damage events (swelling, blebbing) that extend spatially at up to micrometer distances and ultimately lead to debris.

A striking feature of this study is that in apparently normal myelin sheaths, even though the macroscopic morphology is similar from score to score, molecular scale lipid disorder increases with the EAE disease progression. This result emphasizes the potential of PR-CARS to reveal features that are not visible at a macroscopic scale, which is particularly interesting in the context of the monitoring of the evolution of a pathology. Note that normal myelin can be easily identified regardless of the clinical score, and could thus serve ultimately as a convenient and robust assessment of the disease. This study also shows that in the context of EAE, the more traditionally used *g*-ratio factor, which is based on macroscopic-scale morphological information, seems less robust. Previous works have reported the use of *g* ratio as an assessment of a neuronal condition in straight nerves after crush lesion (28,46) or chemically induced demyelination (29,49). In spinal cord or brain samples, however, a number of shape abnormalities are detected (27), which make the measurement of *g* ratio more delicate and potentially biased.

CONCLUSIONS

In this work, we have shown the possibility to probe, by PR-CARS, lipid orientational organization at the molecular level within the myelin sheath of mice spinal cord tissues, in the frame of demyelination and neurodegeneration. Modifications of lipid order have been found in myelin structures that seem morphologically unaffected at the macroscopic scale, emphasizing the possibility of the technique to decipher processes that occur at early stages of demyelination. The higher degradation of lipid order has been found in the processes of swelling and blebbing, especially at the inner interface of the myelin sheath, an effect that is strong enough to induce long-range deformations of the whole myelin sheath. This supports early findings that addressed local lipid modifications by biochemical analyses, and advantageously complements such studies by imaging, which provides a way to address those questions potentially in vivo. Although the data are at this stage not spectrally resolved within the CH-based lipids vibration bands, for instance to discriminate saturated versus unsaturated lipids, future directions can be envisioned to study more precisely the origin of the observed phenomena by adding chemical specificity but at the expense of lower signal levels. Ultimately if applied in vivo, this methodology could serve as an early stage detection for demyelinating diseases progression. Such developments could benefit from recent progresses in in vivo nonlinear imaging through an implanted spinal cord window (50) or CARS endoscopy modalities (51,52).

SUPPORTING MATERIAL

Supporting Materials and Methods and five figures are available at http://www.biophysj.org/biophysj/supplemental/S0006-3495(17)30870-6.

AUTHOR CONTRIBUTIONS

P.G. performed the experiments, prepared all MLV samples, and analyzed data. A.J. and F.D. prepared all spinal cord samples. F.-Z. B. developed data analysis tools. N.K.B., H.B.d.A, J.D., P.F., and H.R. contributed to analysis tools and experimental developments. S.B. designed research and analytic tools. P.G., S.B., and F.D. wrote the manuscript.

ACKNOWLEDGMENTS

We thank D. Côté and A. Gasecka (Université Laval, Quebec, Canada) for providing the spinal cord slices used for birefringent measurements described in the Supporting Material.

This work has been supported by Centre National de la Recherche Scientifique (CNRS), contracts ANR-15-CE19-0018-01 (MyDeepCARS), ANR-10-INBS-04-01 (France-BioImaging), ANR-11-INSB-0006 (France Life Imaging), and Conseil Regional Provence Alpes Côte d'Azur. F.-Z.B. received a scholarship from the Erasmus Mundus Doctorate Program Europhotonics (grant no. 159224-1-2009-1-FR-ERA MUNDUS-EMJD).

SUPPORTING CITATIONS

References (53–56) appear in the Supporting Material.

REFERENCES

1. Morell, P., and R. H. Quarles. 1999. Myelin formation, structure and biochemistry. *In* Basic Neurochemistry: Molecular, Cellular and Medical Aspects, 7th Ed. G. J. Siegel, R. W. Albers, S. T. Brady, and D. L. Price, eds. Elsevier/Academic Press, San Diego, CA, pp. 51–71.
2. Aggarwal, S., L. Yurlova, and M. Simons. 2011. Central nervous system myelin: structure, synthesis, and assembly. *Trends Cell Biol.* 21:585–593.
3. Moore, G. R. 2010. Current concepts in the neuropathology and pathogenesis of multiple sclerosis. *Can. J. Neurol. Sci.* 37 (*Suppl 2*): S5–S15.
4. van der Valk, P., and S. Amor. 2009. Preactive lesions in multiple sclerosis. *Curr. Opin. Neurol.* 22:207–213.
5. Dalcanto, M. C., H. M. Wiśniewski, …, C. S. Raine. 1975. Vesicular disruption of myelin in autoimmune demyelination. *J. Neurol. Sci.* 24:313–319.
6. Lassmann, H., and H. M. Wisniewski. 1979. Chronic relapsing experimental allergic encephalomyelitis: morphological sequence of myelin degradation. *Brain Res.* 169:357–368.
7. Lassmann, H., H. P. Ammerer, and W. Kulnig. 1978. Ultrastructural sequence of myelin degradation. I. Wallerian degeneration in the rat optic nerve. *Acta Neuropathol.* 44:91–102.
8. Genain, C. P., B. Cannella, …, C. S. Raine. 1999. Identification of autoantibodies associated with myelin damage in multiple sclerosis. *Nat. Med.* 5:170–175.
9. Inouye, H., J. Liu, …, D. A. Kirschner. 2014. Myelin organization in the nodal, paranodal, and juxtaparanodal regions revealed by scanning x-ray microdiffraction. *PLoS One.* 9:e100592.
10. Poccia, N., G. Campi, …, A. Bianconi. 2014. Changes of statistical structural fluctuations unveils an early compacted degraded stage of PNS myelin. *Sci. Rep.* 4:5430.
11. Ohler, B., K. Graf, …, C. Husted. 2004. Role of lipid interactions in autoimmune demyelination. *Biochim. Biophys. Acta.* 1688:10–17.
12. Banquy, X., K. Kristiansen, …, J. N. Israelachvili. 2012. Adhesion and hemifusion of cytoplasmic myelin lipid membranes are highly dependent on the lipid composition. *Biochim. Biophys. Acta.* 1818:402–410.
13. Fu, Y., T. J. Frederick, …, J. X. Cheng. 2011. Paranodal myelin retraction in relapsing experimental autoimmune encephalomyelitis visualized by coherent anti-Stokes Raman scattering microscopy. *J. Biomed. Opt.* 16:106006.
14. Wang, H., Y. Fu, …, J. X. Cheng. 2005. Coherent anti-stokes Raman scattering imaging of axonal myelin in live spinal tissues. *Biophys. J.* 89:581–591.
15. Min, Y., T. F. Alig, …, J. A. Zasadzinski. 2011. Critical and off-critical miscibility transitions in model extracellular and cytoplasmic myelin lipid monolayers. *Biophys. J.* 100:1490–1498.
16. Lee, D. W., Y. Min, …, J. A. Zasadzinski. 2011. Relating domain size distribution to line tension and molecular dipole density in model cytoplasmic myelin lipid monolayers. *Proc. Natl. Acad. Sci. USA.* 108:9425–9430.
17. Lee, D. W., X. Banquy, …, J. N. Israelachvili. 2014. Lipid domains control myelin basic protein adsorption and membrane interactions between model myelin lipid bilayers. *Proc. Natl. Acad. Sci. USA.* 111:E768–E775.
18. Baumgart, T., S. Das, …, J. T. Jenkins. 2005. Membrane elasticity in giant vesicles with fluid phase coexistence. *Biophys. J.* 89:1067–1080.
19. Ben Arous, J., J. Binding, …, L. Bourdieu. 2011. Single myelin fiber imaging in living rodents without labeling by deep optical coherence microscopy. *J. Biomed. Opt.* 16:116012.

20. Schain, A. J., R. A. Hill, and J. Grutzendler. 2014. Label-free in vivo imaging of myelinated axons in health and disease with spectral confocal reflectance microscopy. *Nat. Med.* 20:443–449.

21. Farrar, M. J., F. W. Wise, …, C. B. Schaffer. 2011. In vivo imaging of myelin in the vertebrate central nervous system using third harmonic generation microscopy. *Biophys. J.* 100:1362–1371.

22. Lim, H., D. Sharoukhov, …, C. V. Melendez-Vasquez. 2014. Label-free imaging of Schwann cell myelination by third harmonic generation microscopy. *Proc. Natl. Acad. Sci. USA.* 111:18025–18030.

23. Zumbusch, A., G. R. Holtom, and X. S. Xie. 1999. Three-dimensional vibrational imaging by coherent anti-Stokes Raman scattering. *Phys. Rev. Lett.* 82:4142–4145.

24. Evans, C. L., and X. S. Xie. 2008. Coherent anti-stokes Raman scattering microscopy: chemical imaging for biology and medicine. *Annu. Rev. Anal. Chem. (Palo Alto, Calif.).* 1:883–909.

25. Yu, Y., P. V. Ramachandran, and M. C. Wang. 2014. Shedding new light on lipid functions with CARS and SRS microscopy. *Biochim. Biophys. Acta.* 1841:1120–1129.

26. Fu, Y., T. B. Huff, …, J. X. Cheng. 2008. Ex vivo and in vivo imaging of myelin fibers in mouse brain by coherent anti-Stokes Raman scattering microscopy. *Opt. Express.* 16:19396–19409.

27. Imitola, J., D. Côté, …, S. J. Khoury. 2011. Multimodal coherent anti-Stokes Raman scattering microscopy reveals microglia-associated myelin and axonal dysfunction in multiple sclerosis-like lesions in mice. *J. Biomed. Opt.* 16:021109.

28. Bélanger, E., F. P. Henry, …, D. Côté. 2011. In vivo evaluation of demyelination and remyelination in a nerve crush injury model. *Biomed. Opt. Express.* 2:2698–2708.

29. de Vito, G., I. Tonazzini, …, V. Piazza. 2014. RP-CARS: label-free optical readout of the myelin intrinsic healthiness. *Opt. Express.* 22:13733–13743.

30. Bélanger, E., S. Bégin, …, D. Côté. 2009. Quantitative myelin imaging with coherent anti-Stokes Raman scattering microscopy: alleviating the excitation polarization dependence with circularly polarized laser beams. *Opt. Express.* 17:18419–18432.

31. Shi, Y., D. Zhang, …, J. X. Cheng. 2011. Longitudinal in vivo coherent anti-Stokes Raman scattering imaging of demyelination and remyelination in injured spinal cord. *J. Biomed. Opt.* 16:106012.

32. Bégin, S., E. Bélanger, …, D. Côté. 2013. Local assessment of myelin health in a multiple sclerosis mouse model using a 2D Fourier transform approach. *Biomed. Opt. Express.* 4:2003–2014.

33. Bégin, S., O. Dupont-Therrien, …, D. C. Côté. 2014. Automated method for the segmentation and morphometry of nerve fibers in large-scale CARS images of spinal cord tissue. *Biomed. Opt. Express.* 5:4145–4161.

34. Turcotte, R., D. J. Rutledge, …, D. C. Côté. 2016. Intravital assessment of myelin molecular order with polarimetric multiphoton microscopy. *Sci. Rep.* 6:31685.

35. Berthold, C. H., I. Nilsson, and M. Rydmark. 1983. Axon diameter and myelin sheath thickness in nerve fibres of the ventral spinal root of the seventh lumbar nerve of the adult and developing cat. *J. Anat.* 136:483–508.

36. Brasselet, S. 2011. Polarization resolved nonlinear microscopy: application to structural molecular and biological imaging. *Adv. Opt. Photonics.* 3:205.

37. Munhoz, F., H. Rigneault, and S. Brasselet. 2010. High order symmetry structural properties of vibrational resonances using multiple-field polarization coherent anti-Stokes Raman spectroscopy microscopy. *Phys. Rev. Lett.* 105:123903–123907.

38. de Vito, G., V. Cappello, …, V. Piazza. 2016. RP-CARS reveals molecular spatial order anomalies in myelin of an animal model of Krabbe disease. *J. Biophoton.* 10:385–393.

39. Bioud, F. Z., P. Gasecka, …, S. Brasselet. 2014. Structure of molecular packing probed by polarization-resolved nonlinear four-wave mixing and coherent anti-Stokes Raman-scattering microscopy. *Phys. Rev. A.* 89:013836.

40. Duboisset, J., P. Berto, …, S. Brasselet. 2015. Molecular orientational order probed by coherent anti-Stokes Raman scattering (CARS) and stimulated Raman scattering (SRS) microscopy: a spectral comparative study. *J. Phys. Chem. B.* 119:3242–3249.

41. Bangham, A. D., M. W. Hill, and N. G. A. Miller. 1974. Preparation and use of liposomes as models of biological membranes. *In* Methods in Membrane Biology. E. D. Korn, ed. Springer, Boston, MA, pp. 1–68.

42. Veatch, S. L., and S. L. Keller. 2003. Separation of liquid phases in giant vesicles of ternary mixtures of phospholipids and cholesterol. *Biophys. J.* 85:3074–3083.

43. Ferrand, P. 2015. GPScan.VI: a general-purpose LabVIEW program for scanning imaging or any application requiring synchronous analog voltage generation and data acquisition. *Comput. Phys. Commun.* 192:342–347.

44. Ferrand, P., P. Gasecka, …, S. Brasselet. 2014. Ultimate use of two-photon fluorescence microscopy to map orientational behavior of fluorophores. *Biophys. J.* 106:2330–2339.

45. de Aguiar, H. B., P. Gasecka, and S. Brasselet. 2015. Quantitative analysis of light scattering in polarization-resolved nonlinear microscopy. *Opt. Express.* 23:8960–8973.

46. Knöferle, J., J. C. Koch, …, P. Lingor. 2010. Mechanisms of acute axonal degeneration in the optic nerve in vivo. *Proc. Natl. Acad. Sci. USA.* 107:6064–6069.

47. Min, Y., K. Kristiansen, …, J. Israelachvili. 2009. Interaction forces and adhesion of supported myelin lipid bilayers modulated by myelin basic protein. *Proc. Natl. Acad. Sci. USA.* 106:3154–3159.

48. Kress, A., X. Wang, …, S. Brasselet. 2013. Mapping the local organization of cell membranes using excitation-polarization-resolved confocal fluorescence microscopy. *Biophys. J.* 105:127–136.

49. Fu, Y., H. Wang, …, J. X. Cheng. 2007. Coherent anti-Stokes Raman scattering imaging of myelin degradation reveals a calcium-dependent pathway in lyso-PtdCho-induced demyelination. *J. Neurosci. Res.* 85:2870–2881.

50. Fenrich, K. K., P. Weber, …, F. Debarbieux. 2013. Implanting glass spinal cord windows in adult mice with experimental autoimmune encephalomyelitis. *J. Vis. Exp.* 82:e50826.

51. Brustlein, S., P. Berto, …, H. Rigneault. 2011. Double-clad hollow core photonic crystal fiber for coherent Raman endoscope. *Opt. Express.* 19:12562–12568.

52. Saar, B. G., R. S. Johnston, …, E. J. Seibel. 2011. Coherent Raman scanning fiber endoscopy. *Opt. Lett.* 36:2396–2398.

53. Munhoz, F., S. Brustlein, …, H. Rigneault. 2011. Polarization resolved stimulated Raman scattering: probing depolarization ratios of liquids. *J. Raman Spectrosc.* 43:419–424.

54. de Campos Vidal, B., M. L. S. Mello, …, C. Godo. 1980. Anisotropic properties of the myelin sheath. *Acta Histochem.* 66:32–39.

55. Brasselet, S., D. Aït-Belkacem, …, S. Brasselet. 2010. Influence of birefringence on polarization resolved nonlinear microscopy and collagen SHG structural imaging. *Opt. Express.* 18:14859–14870.

56. Heimburg, T. 2008. Thermal Biophysics of Membranes. Wiley, Berlin, Germany.

Biophysical Journal, Volume *113*

Supplemental Information

Lipid Order Degradation in Autoimmune Demyelination Probed by Polarized Coherent Raman Microscopy

Paulina Gasecka, Alexandre Jaouen, Fatma-Zohra Bioud, Hilton B. de Aguiar, Julien Duboisset, Patrick Ferrand, Herve Rigneault, Naveen K. Balla, Franck Debarbieux, and Sophie Brasselet

Lipid order degradation in autoimmune demyelination probed by polarization resolved coherent Raman microscopy Supporting Material

P. Gasecka, A. Jaouen, F.-Z. Bioud, H. B. de Aguiar, J. Duboisset, P. Ferrand, H. Rigneault, N. K. Balla, F. Debarbieux, and S. Brasselet

1 PR-CARS data analysis

The calculation of the CARS polarized (PR-CARS) response from the lipid assembly present in the focal volume of an objective relies on a bond additive model where individual CH molecular bonds add-up coherently to form a nonlinear susceptibility tensor γ for each vibration mode, responsible for the CARS nonlinear coherent radiation. These bond dipoles directions **e** with orientations (θ, φ) in the macroscopic frame form a macroscopic nonlinear susceptibility tensor $\chi^{(3)}_{IJKL}$ of the lipid assembly in the macroscopic 3D frame (X, Y, Z). It has been shown that since the incident optical field is polarized in the (X, Y) plane, the read-out of the CARS signal occurs from a reduced 2D macroscopic tensor (1):

$$\chi^{(3)}_{IJKL} = N\gamma \int_{\varphi} (\mathbf{I}\cdot\mathbf{e})(\mathbf{J}\cdot\mathbf{e})(\mathbf{K}\cdot\mathbf{e})(\mathbf{L}\cdot\mathbf{e})p(\varphi)d\varphi \tag{1}$$

where $(I, J, K, L) = (X, Y)$. N is the molecular bonds density, γ is the molecular vibration tensor norm, $(\mathbf{I}\cdot\mathbf{e})$ refers to the projection of the **e** vector on the macroscopic frame axis **I**, and $p(\varphi)$ is the orientational distribution function of **e** vectors averaged on their out-of plane orientation (θ) (1). The nonlinear response finally depends on the function $p(\varphi)$, a 2D effective distribution function that can be decomposed over its symmetry orders read by the PR-CARS process:

$$p(\varphi) = p_0 + p_2\cos(2\varphi) + q_2\sin(2\varphi) + p_4\cos(4\varphi) + q_4\sin(4\varphi) \tag{2}$$

where p_0 is the isotropic contribution to the angular distribution, (p_2, q_2) are its second order symmetry components and (p_4, q_4) its fourth order symmetry components. Relations between the macroscopic nonlinear susceptibility terms ($\chi^{(3)}_{XXXX}, \chi^{(3)}_{XXXY}$...) and the angular distribution function parameters ((p_2, q_2), ...) can be found in (1).

In the PR-CARS analysis, both incident pump field (E_p) and Stokes field (E_s) are linearly polarized and rotated with a variable angle α relative to the sample plane horizontal axis X. The CARS intensity can be written as (1):

$$I^{CARS}_{I}(\alpha) \quad \propto \quad \sum_{\substack{JKL \\ MNO}} \chi^{(3)}_{IJKL}\chi^{(3)*}_{IMNO}E_{p,J}E_{p,K}E^{*}_{s,L}E^{*}_{p,M}E^{*}_{p,N}E_{s,O}(\alpha). \tag{3}$$

where $E_{p,J}(\alpha)$ is the projection of the pump incident field on the axis **J** in the sample plane. In the PR-CARS data analysis, the total CARS intensity is decomposed on a circular basis:

$$\begin{aligned} I^{CARS}(\alpha) \quad \propto a_0 \quad & +a_2\cos(2\alpha) + b_2\sin(2\alpha) + a_4\cos(4\alpha) + b_4\sin(4\alpha) \\ & +a_6\cos(6\alpha) + b_6\sin(6\alpha), \end{aligned} \tag{4}$$

where the (a_n, b_n) coefficients are directly calculated from the recorded polarization dependent image stack by projection on circular basis functions.

The (p_n, q_n) parameters are deduced from these coefficients following the relations (1, 2):

$$\begin{aligned} a_0 &= \tfrac{1}{64}(36p_0^2 + 10p_2^2 + 10q_2^2 + p_4^2 + q_4^2) \\ a_2 &= \tfrac{1}{32}(24p_0p_2 + 3p_2p_4 + 3q_2q_4);\ b_2 = \tfrac{1}{32}(p_0q_2 + 3p_2q_4 - 3p_4q_2) \\ a_4 &= \tfrac{3}{32}(p_2^2 - q_2^2 + 2p_0p_4);\ b_4 = \tfrac{3}{16}(2p_0q_4 + p_2q_2) \\ a_6 &= \tfrac{1}{32}(p_2p_4 - q_2q_4);\ b_6 = \tfrac{1}{32}(p_2q_4 + p_4q_2) \end{aligned} \tag{5}$$

© 2013 The Authors
0006-3495/08/09/2624/12 $2.00

2 Sources of error and bias in PR-CARS measurements

Stringent control of the PR-CARS signal conditions are required in order to ensure the validity of the measured order parameters. In this part the different sources of error and bias are investigated.

2.1 Noise

First, S_2, S_4 values are only collected for high-enough intensity values, that guaranty sufficiently low bias and low noise (Fig. S1). Above 1300 analog signal value, standard deviations are of 0.02 for S_2 and 0.08 for S_4. This intensity value will be set as a threshold for all quantitative studies. Above this threshold, we also observe that the S_2 bias is negligible. Concerning S_4, the residual bias (which does not surpass 0.15 with the chosen intensities) is systematically removed from all measured values, accounting for the local pixel intensities and the reference noise-intensity dependence depicted (Fig. S1). In conclusion by using intensity thresholding, the measured parameters are relevant for statistical analysis and hence for comparison between different myelin regions and scores.

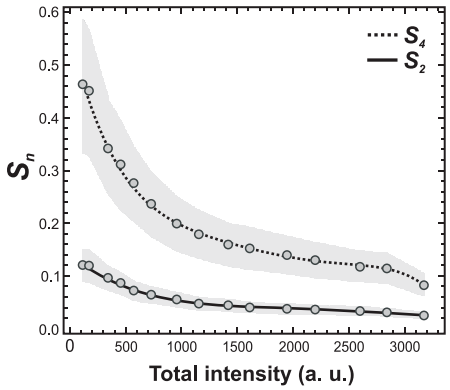

Figure S1: S_2 and S_4 dependence on the CARS intensity signal (summed over 18 input polarization angles) in the isotropic medium. The shaded region represents the standard deviation of the mean S_2 and S_4 values.

2.2 Non-resonant background

Second, some care has to be taken regarding the existence of non-resonant background in the data. Considering our previous studies performed on model multilamellar lipid membrane vesicles, it is obvious that the non-resonant Four Wave Mixing (FWM) signal can lead to an underestimation of S_2 (2). The difference between measured values and background-free ones (measured in absence of non-resonant background by Stimulated Raman Scattering (SRS)) have been estimated to be about 0.2 in multilamellar vesicles (MLVs) made of dipalmitoylphosphatidylcholine (DPPC), S_4 being almost un-affected (2). In this work we display raw data, however it is worth noting that the background-free S_2 values have to be increased by an offset, which is most probably not higher than 0.2, considering that MLVs data are very close to values measured in myelin (see below).

2.3 Out of plane mean orientation

Third, (S_2, S_4) values depend on possible out-of-plane orientations of the observed distributions. All the models developed in this work assume that the molecular angular distributions are lying in the sample plane. In order to properly report structural properties of myelinated axons, one needs to ensure that the PR-CARS measurement is performed at the equatorial plane of the axon/myelin tube. Any out-of-plane orientation of the observed distribution can indeed bias the results interpretation by adding a component which tends towards isotropy. In order to estimate how the (S_2, S_4) order parameters depend on this

effect in the myelin sheath, we performed PR-CARS measurements at several focusing planes (Z steps every 0.5 μm) crossing the whole 3D tubular structure of the myelin sheath from bottom to top (Fig. S2). S_2 seems to be robust with negligible

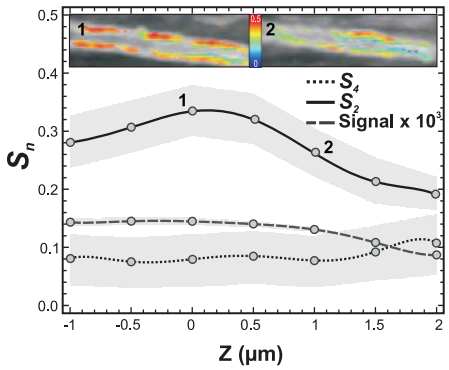

Figure S2: S_2 and S_4 mean values measured on a myelin sheath as a function of the sample depth Z. The shaded regions indicate the standard deviation of the order parameters (over all pixels in selected regions along the myelin sheath, according to an intensity thresholding of 75% of the maximum intensity measured in the image). Z$=0$ corresponds to the depth of the myelin tube equatorial plane. Insets: S_2 images after intensity thresholding, at Z$=0$ (point 1) and 1 μm above (point 2). Both images are superimposed with the CARS intensity images in grayscale.

modification over a defocus of ± 5 μm around the equatorial plane. This means that as long as the myelin sheath looks visually in focus (which is the case for this defocus range), the S_2 measurement is reliable. Moreover its standard deviation does not depend on Z. S_4 on the other hand is very robust to a defocus change, which is consistent with the fact that defocus changes the apparent disorder of the distribution, not its shape. The only noticeable changes of S_4 are a slight increase at the largest depth of focus, however in this region the intensity also drops down, which might increase the bias on S_4.

2.4 Birefringence

At last, the measured S_2 values can also be underestimated if the sample exhibits birefringence. Birefringence acts indeed as a distortion for excitation fields' polarization state, making them elliptic and tilted relative to their expected directions (3). Birefringence is known to be non-negligible in the myelin sheath, due to the tight and regular arrangement of lipids (4). We estimated the birefringence phase shift in myelin sample slices of thicknesses of about 30 μm in order to extrapolate the expected birefringence in the measured spinal cord tissues (Fig. S3). The slices were cut after extraction and fixation in the sagittal plane using a vibratome, and placed in phosphate-buffered saline (PBS).

The measurement of birefringence follows a method presented in (1, 5, 6) (Fig. S3). A laser beam ($\lambda = 800$ nm) is focused on the sample surface using the same microscope as used in PR-CARS. The incident linear polarization is rotated with an angle α (relative to the horizontal sample plane direction X) from $0°$ to $170°$ with a step of $10°$. The transmitted intensity modulation is recorded on a photomultiplier, placed after a polarizer of horizontal orientation (e.g. along the X direction of the sample plane, denoted (X, Y)). As a control in a non-birefringent sample, we performed the same experiment next to the spinal cord slice tissue in PBS. The resulting intensity polarization response along the X and Y analyzer directions can be written as quantities proportional to:

$$\begin{aligned} I_X(\alpha) &= |E_X(\alpha)|^2 \\ I_Y(\alpha) &= |E_Y(\alpha)|^2 \end{aligned}$$

where $E_{X,Y}$ are the transmitted field components along the X and Y directions respectively. Here only $I_X(\alpha)$ is measured. If birefringence occurs locally in a sample of given thickness, along a given optical axis direction Θ (typically the local direction of lipid chains in a thick multi-layer membrane), then the fields' components along this axis and its perpendicular direction will be phase-shifted by a value Φ. Before reaching the birefringent medium, the optical electric fields are written $(E_X, E_Y) = (\cos\alpha, \sin\alpha)$ in the laboratory frame. The birefringence imposes a phase shift Φ between the component of the

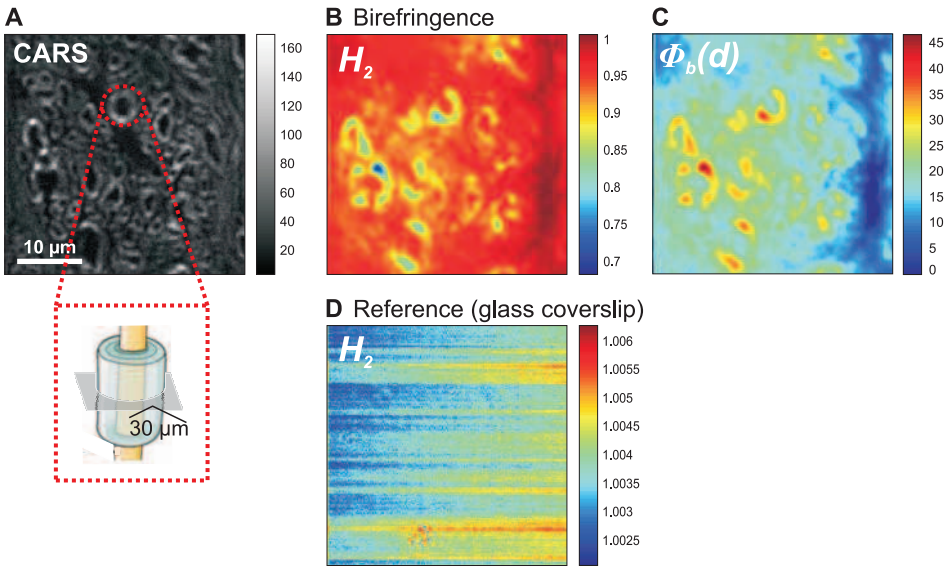

Figure S3: (***a***) CARS image (2845 cm^{-1}) of a spinal cord slice (mean thickness = 30 μm) on the region where the birefringence has been measured. (***b***) Measured H_2 map from the polarized signal measured on the spinal cord slice (in this scheme, values are not relevant for optical axes oriented along the horizontal and vertical orientations, see text). (***c***) Deduced birefringence Φ map of the deduced birefringence value. (***d***) Measured H_2 map from the signal measured on a glass coverslip.

field along the slow optical axis of the birefringent medium (denoted X_b) and its fast axis (denoted Y_b), such as:

$$\begin{aligned} E_{X_b}(\alpha,\Theta,\Phi) &= (\cos\alpha\,\cos\Theta+\sin\alpha\,\sin\Theta)\,e^{i\Phi} \\ E_{Y_b}(\alpha,\Theta,\Phi) &= (-\cos\alpha\,\sin\Theta+\sin\alpha\,\cos\Theta) \end{aligned}$$

Transforming this expression back in the sample plane frame (X,Y), the field components are written

$$\begin{aligned} E_X(\alpha,\Theta,\Phi) &= E_{X_b}(\alpha,\Theta,\Phi)\,\cos\Theta - E_{Y_b}(\alpha,\Theta,\Phi)\,\sin\Theta \\ E_Y(\alpha,\Theta,\Phi) &= E_{X_b}(\alpha,\Theta,\Phi)\,\sin\Theta + E_{Y_b}(\alpha,\Theta,\Phi)\,\cos\Theta \end{aligned}$$

The new intensity $I_X(\alpha,\Theta,\Phi)=|E_X(\alpha,\Theta,\Phi)|^2$ dependence can be easily decomposed into circular functions such as:

$$I_X(\alpha,\Theta,\Phi) = a_0(\Theta,\Phi)+a_2(\Theta,\Phi)\cos(2\alpha)+b_2(\Theta,\Phi)\sin(2\alpha) \quad (6)$$

with:

$$\begin{aligned} a_0(\Theta,\Phi) &= 1/2 \\ a_2(\Theta,\Phi) &= 1/2(1-\sin^2(2\Theta)(1-\cos\Phi)) \\ b_2(\Theta,\Phi) &= 1/4\sin(4\Theta)(1-\cos\Phi) \end{aligned}$$

We can define the magnitude and phase of this modulation as:

$$\begin{aligned} H_2(\Theta,\Phi) &= \tfrac{1}{a_0(\Theta,\Phi)}\sqrt{(a_2(\Theta,\Phi)^2+b_2(\Theta,\Phi)^2)} \\ \phi_2(\Theta,\Phi) &= 1/2\arctan(b_2(\Theta,\Phi)/a_2(\Theta,\Phi)) \end{aligned}$$

In an isotropic medium, the measured modulation is proportional to $\cos^2(\alpha)$, since there is no perturbation of the incident polarization state. The resulting expected values are thus $H_2 = 1$ and $\phi_2 = 0[\pi/2]$. In a birefringent sample $H_2=\sqrt{\cos^2(4\Theta)+\sin^2(4\Theta)\cos^2(\Phi)}$ and therefore H_2 is directly related to the birefringence phase shift Φ and the main birefringence axis direction Θ; it is generally lower than 1, except if $\Phi = 0[\pi]$, which means no birefringence, or a birefringence value which is an integer number of π. The fact that $H_2 \leq 1$ is due to the existence of ellipticity, induced by Φ. In order to extract the quantities (Φ,Θ) from the new measured modulation, some operations need to be performed on the modulation parameters (a_2,b_2):

$$\begin{aligned} \cos(\Phi) &= \arccos(1-\tfrac{2\,b_2}{\sin(4\Theta)}) \\ \tan(2\Theta) &= \tfrac{1-a_2}{b_2} \end{aligned}$$

The quantity Φ is thus extracted modulo π, while Θ is extracted modulo $\pi/2$. Note however that due to the measurement geometry (fixed analyzer axis), these quantities cannot be measured for $\Theta = 0[\pi/2]$. A rotation of the analyzer is necessary to disentangle this indetermination.

Values of H_2 calculated from the transmitted signal through the spinal cord sample are depicted in Fig. S3b. H_2 is clearly lower than 1 in many places of the sample, principally concentrated on the myelin sheath contours. The deduced phase shift Φ is shown in Fig. S3c. In this image, the birefringence can be quantified in regions of the myelin sheaths that do not correspond to orientations of the lipids around $0°$ or $90°$, for the reason indicated above.

The resulting Φ values range from $20°$ to $40°$for the 30 μm (on average) thick slice of the spinal cord sample, which indicates that the sample birefringence is quite large, as also previously reported in the literature. In comparison, the reference glass coverslip H_2 is very close to 1 as can be seen in Fig. S3d.

The found birefringence phase shift extrapolated for a depth of penetration of 30 μm (maximum focus depth used here) is therefore in the range of $20°$ to $40°$. The induced polarization distortions have been included in a model of the myelin sheath response (using input (S_2, S_4) values close to the measured ones), following the method described in (1). The birefringence values are seen to induce a negligible bias of (< 0.05) for S_2, and of 0.05 for S_4. Even though the myelin birefringence is non negligible, the shallow depth penetration used here allows neglecting this effect. However, it means that care has to be taken in case of future investigations at deeper penetration distances.

3 Molecular order in model lipid membranes

PR-CARS data were recorded in the spectral region averaged around the CH_2 symmetric stretching vibration. We considered MLVs having comparable intensity and size in the range from 5 to 30 μm, and imaged both "filled" and "non-filled" MLVs that were encountered in the samples (Fig. S4a, b).

In order to compare the organization of lipids in both populations, we considered only pixels taken from their border in the equatorial plane. (S_2, φ_2) images exhibit a strong orientational dependence of lipids in the equatorial plane of MLVs as compared to the isotropic aqueous solution, with CH bonds oriented along the membrane contour (Fig. S4c). The highest degree of the lipid order was found for non-filled MLVs made of DPPC lipids, with $\langle S_2 \rangle \approx 0.40$ and $\langle S_4 \rangle \approx 0.06$ (all averages are given over measurements performed over 5 to 10 MLVs). This corresponds to an effective distribution function resembling a Gaussian with an aperture $\sigma \approx 70°$ (Fig. S4d). Filled MLVs exhibit a higher disorder (Fig. S4d) ($\langle S_2 \rangle \approx 0.29$ and $\langle S_4 \rangle \approx 0.05$), most probably because of the lower tension exerted on the outer membranes due to the disorganized inner lipid layers. The measured order can change dramatically with different types of lipids, in particular their degree of saturation. Non-filled MLVs made of DOPC lipids exhibit a lower order with $\langle S_2 \rangle \approx 0.23$, with S_4 almost unchanged (Fig. S4e). This reflects the fact that at room temperature, DPPC is in the gel phase while DOPC is in the liquid disordered phase, with more possible conformational changes that leads to higher disorder (7).

4 Measurement of the g-ratio

The g-ratio is given by the ratio between the inner to the outer diameter of the myelin membrane (Fig. S5).

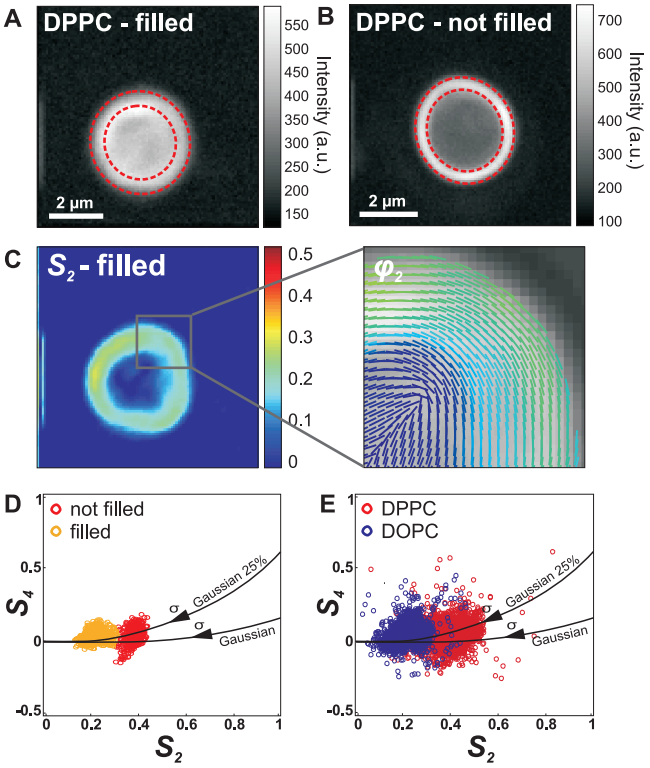

Figure S4: PR-CARS analysis on model multilamellar vesicles (MLVs) (around 2845 cm^{-1}). (***a***): intensity CARS image of the 'filled' MLVs made of pure DPPC. The dashed circles delimitate the region of analysis, emphasizing the outer edge of the MLV. (***b***) similar image for a 'not filled' DPPC MLV. (***c***) map of S_2 values (left) and corresponding φ_2 image showing the mean orientation of CH molecular bonds (right). (***d***) Comparison of (S_2, S_4) values in 'filled' and 'not filled' DPPC MLVs (each point is a pixel taken between dashed circles represented in the intensity images). (***e***) Comparison of (S_2, S_4) values in MLVs made of either pure DPPC or pure DOPC lipids. Continuous lines represent models from a pure Gaussian distribution and a Gaussian distribution superimposed with an isotropic distribution with a proportion of 25%.

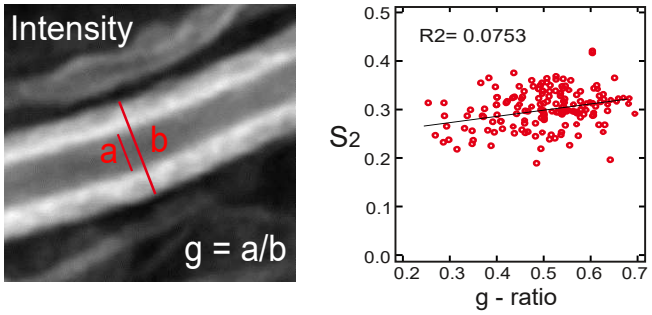

Figure S5: Measurement of the g-ratio in the equatorial plane of a myelin sheath, using the total intensity CARS image (a: inner diameter, b: outer diameter, g-ratio is the ratio between the inner and outer diameters). Mean $< S_2 >$ values of all measurements versus g-ratio on all , with linear interpolation and correlation coefficient of the fit.

5 Supporting References

References

1. Bioud, F. Z., and P. Gasecka, and P. Ferrand, and H. Rigneault, and J. Duboisset, and S. Brasselet. 2014. Structure of molecular packing probed by polarization-resolved nonlinear four-wave mixing and coherent anti-Stokes Raman-scattering microscopy. *Phys. Rev. A.*

89:013836–013846.
2. Duboisset, J., and P. Berto, and P. Gasecka, and F. Z. Bioud, and P. Ferrand, and H. Rigneault, and S. Brasselet. 2015. Molecular orientational order probed by coherent anti-Stokes Raman scattering (CARS) and stimulated Raman scattering (SRS) microscopy: A spectral comparative study. *J. Phys. Chem. B.* 119:3242–3249.
3. Munhoz, F., and S. Brustlein, and R. Hostein, and P. Berto, and S. Brasselet, and H. Rigneault. 2012. Polarization resolved stimulated raman scattering: probing depolarization ratios of liquids. *J. Raman Spectrosc.* 43:419–424.
4. De Campos Vidal, B., and M. L. S. Mello, and A. C. Caseiro-Filho, and C. Godo. 1980. Anisotropic properties of the myelin sheath. *Acta histochem.* 66:32–39.
5. Munhoz, F., and H. Rigneault, and S. Brasselet. 2010. High order symmetry structural properties of vibrational resonances using multiple-field polarization coherent anti-Stokes Raman spectroscopy microscopy. *Phys. Rev. Lett.* 105:123903–123907.
6. Aït-Belkacem, D., and A. Gasecka, and F. Munhoz, and S. Brustlein, and S. Brasselet. 2010. Influence of birefringence on polarization resolved nonlinear microscopy and collagen SHG structural imaging. *Opt. Express.* 18:14859–14870.
7. Heimburg, T. 2008. Thermal biophysics of membranes. Wiley-VCH, Berlin.

List of Figures